Wave-equation migration Q analysis (WEMQA)

Yi Shen

ABSTRACT

Estimates of quality factor Q are useful in seismic processing, amplitude analysis, and reservoir characterization. However, Q model building, which is conventionally done in the data space using ray-based tomography, is a notoriously challenging problem due to issues like spectral interference, low signal-to-noise ratio, diffractions, and complex subsurface structure. To produce a reliable Q model, we present a new approach with two major features. First, this method is performed in the image-space, which uses downward-continuation imaging with Q to stack out noise, focus and simplify events, and provide a direct link between the model perturbation and the image perturbation. We develop two methods to generate the image perturbation for the following scenarios: the model with sparse reflectors and the model with dense reflectors. Second, this method uses wave-equation Q tomography to handle the complex wave propagation. Two synthetic tests on two different 2-D models with a Q anomaly shows the capability of this method on the model with sparse events. Tests with a modified SEAM model also demonstrate the feasibility of this method for the model with dense events.

INTRODUCTION

Attenuation, parametrized by seismic quality factor, Q, causes high frequencies loss and phase distortion of surface seismic reflection data. An understanding of the effects and properties of this attenuation parameter has two major motivations. First, Q is a useful parameter for characterizing rock and fluid properties–e.g., saturation, porosity, permeability, and viscosity–because of its high sensitivity to some of these properties (e.g. Best et al. (1994)). Second, if the absorption properties of the subsurface are known, they can be included in seismic data processing (deconvolution, stacking, migration, inverse Q filtering, etc.) to get images with higher qualities, and to better interpret the effects of AVO and anisotropy, which also have offset-dependent signatures.

Studies of estimating attenuation tomographically have a long history. Brzostowski and McMechan (1992), and Leggett et al. (1992) used tomographic estimation of attenuation according to the seismic amplitude changes. Kjartansson (1979), and Zucca et al. (1994) measured the rise time of the broadened wavelets caused by attenuation for Q tomography. Tonn (1991), Quan and Harris (1997), Dasgupta and

Clark (1998), Leaney (1999), Mateeva (2003), Plessix (2006), Rickett (2006), Rickett (2007), Reine et al. (2012a), and Reine et al. (2012b) performed the estimation based on the attenuation-induced spectral changes. However, there are three main difficulties that cause the estimated Q model from these methods to be unreliable. First, Q tomography schemes in these works are mostly ray-based, measuring the spectral changes over different lengths of raypaths, which are prone to errors and unrealistic results when multi-pathing exists in areas of complex overburden. Second, measurements conducted in these works are all in the data domain, which has a number of issues that can affect the accuracy of Q model building. Specifically, diffractions and poor signal-to-noise ratio introduce large errors in Q estimation. In addition, the data domain has an amount of crossed events , which will introduce spectral interference.

Therefore, we produce a reliable Q model by using wave-equation migration Q analysis (WEMQA). This idea is similar to wave-equation migration velocity analysis (WEMVA) (Sava and Biondi, 2004; Biondi, 2006), relates image perturbation with velocity perturbation using wave-equation based tomography. Once the complex wave propagation (i.e. multipathing) presents, wavefield-continuation methods yield better images than ray-based methods, due to their ability to handle multipathing of the reflected energy. Moreover, the data-space approach is vulnerable when the data are contaminated with noise, diffractions and crossing events; whereas the image-space approach is stable, because migration suppresses the noise and focuses the events. To some degree, the migration-based technique is also more efficient than the data-based one, since it can be implemented in a target-oriented fashion and hence focus on the attenuated zone.

In this paper, we first present downward-continuation imaging with Q to provide the basis for image-based Q tomography. Second, we present a wave-equation Q tomography operator – that provides a direct mapping between the change in the image space and the change in the Q model. The change in the image will be discussed afterwards, which can be measured either by computing the difference between the attenuated image and the attenuation-free stacked image, or by computing the spectral variation of each window over depth and image points.

THEORY

Downward-continuation imaging with Q

Valenciano et al. (2011) presented a one-way viscoacoustic wave-equation approach that can accurately migrate data in media with attenuation. Their approach uses an extension of the Fourier Finite-Differences(FFD) algorithm to compensate for the effects of Q during migration. Due to the relatively large frequency dispersion for FFD, we extend the explicit split-step algorithm to migrate the attenuated data.

In a linear attenuating medium, the one-way wave equation used for migration by wavefield continuation has the following phase-shift recursive solution:

$$P_{z+\Delta z}\left(\omega, k_x, k_y\right) = P_z\left(\omega, k_x, k_y\right) e^{\pm i k_z \Delta z}. \tag{1}$$

where P is the pressure, ω is the temporal frequency, k_x and k_y are the horizontal wavenumbers, and k_z is the vertical wavenumber. The plus and minus signs in the phase-shift operator represent downgoing and upgoing waves, respectively.

The vertical wavenumber can be expressed by the following dispersion relation, which is often called the Single Square Root (SSR) equation:

$$k_z = \sqrt{(\omega\tilde{s})^2 - |\mathbf{k}|^2}, \tag{2}$$

where $|\mathbf{k}| = \sqrt{k_x^2 + k_y^2}$; $\tilde{s}$ is the phase slowness, which becomes a complex number and can be given by following equation based on the nearly constant-Q model (Futterman, 1962),

$$\tilde{s}(\omega) = s_{\omega r}\left(1 - \frac{1}{\pi Q}\ln(\omega/\omega_r)\right)\left(1 + \frac{i}{2Q}\right), \tag{3}$$

where $s_{\omega r}$ is the slowness at a reference frequency ω_r. Since attenuation delays more at the lower frequencies than the higher frequencies, I will take the infinite frequency as the reference frequency (the Nyquist frequency in the real case).

The phase-shift migration operator described above is strictly valid for a subsurface model that varies only with depth. To extend the operator to handle laterally varying earth models, a simplified form of this SSR can be approximated by using Taylor expansion around the reference slowness $\tilde{s}_0$ and the reference quality factor Q_0:

$$k_z(s_{\omega r}, Q) = k_{z0}(\tilde{s}_0) + \omega\left(\tilde{s} - \tilde{s}_0\right), \tag{4}$$

where

$$\tilde{s}_0 = s_{\omega r 0}\left(1 - \frac{1}{\pi Q_0}\ln(\omega/\omega_r)\right)\left(1 + \frac{i}{2Q_0}\right). \tag{5}$$

Equation 4 describes split-step migration, whose accuracy can be improved by using more than one reference slowness and Q. In this modified scheme, called Extended Split-Step migration, multiple reference wavefields are generated for interpolatation.

Wave-equation Q tomography operator

Wave-equation Q tomography is a non-linear inversion process that aims to find the Q model that minimizes the residual field in the image space. In general, the residual image, $\Delta\mathbf{I}$, is the difference between the background image computed with the current background Q model, and the 'target' image that will be fully discussed in the later section. This residual image can also be approximated by a linearized operator—wave-equation Q tomography operator $\mathbf{T}$—being performed on the model perturbation $\Delta\mathbf{Q}$:

$$\Delta\mathbf{I} = \mathbf{T}\Delta\mathbf{Q}. \tag{6}$$

The adjoint of this tomographic operator $\mathbf{T}^*$ backprojects the image perturbation into the Q model space, and the back-projected changes in the model space will be used as gradient directions to conduct a line-search in optimization schemes. This backprojection can be expressed as

$$\Delta\mathbf{Q} = \mathbf{T}^*\Delta\mathbf{I}. \tag{7}$$

In this paper, I evaluate this wave-equation tomographic operator $\mathbf{T}$ in the shot-profile domain. Both source and receiver wavefields are downward continued in the shot-profile domain using the one-way wave equations (Claerbout, 1971):

$$\begin{cases} \left(\frac{\partial}{\partial z} + ik_z\right) D(\mathbf{x}, \mathbf{x}_s) = 0 \\ D(x, y, z = 0, \mathbf{x}_s) = f_s\delta(\mathbf{x} - \mathbf{x}_s) \end{cases}, \tag{8}$$

and

$$\begin{cases} \left(\frac{\partial}{\partial z} - ik_z\right) U(\mathbf{x}, \mathbf{x}_s) = 0 \\ U(x, y, z = 0, \mathbf{x}_s) = P(x, y, z = 0, \mathbf{x}_s) \end{cases}, \tag{9}$$

where $D(\mathbf{x}, \mathbf{x}_s)$ is the source wavefield at the image point $\mathbf{x} = (x, y, z)$ with the source located at $\mathbf{x}_s = (x_s, y_s, 0)$; $U(\mathbf{x}, \mathbf{x}_s)$ is the receiver wavefield at the image point $\mathbf{x}$ with the source located at $\mathbf{x}_s$; f_s is the source signature, and $f_s\delta(\mathbf{x} - \mathbf{x}_s)$ defines the point source function at $\mathbf{x_s}$, which serves as the boundary condition of equation 8; $P(x, y, z = 0, \mathbf{x}_s)$ is the recorded shot gather at $\mathbf{x}_s$, which serves as the boundary condition of Equation 9; and k_z is the same vertical wavenumber as shown in Equation 2.

The background image is computed by applying the cross-correlation imaging condition:

$$I(\mathbf{x}, \mathbf{h}) = \sum_{\mathbf{x}_s}\sum_{\omega} \overline{D(\mathbf{x} - \mathbf{h}, \mathbf{x}_s)}U(\mathbf{x} + \mathbf{h}, \mathbf{x}_s), \tag{10}$$

where the bar stands for the complex conjugate, and $\mathbf{h} = (h_x, h_y, h_z)$ is the subsurface half-offset.

Under the Born approximation, a perturbation in the model parameters causes a first-order perturbation in the wavefields. Consequently, the resulting image perturbation reads:

$$\begin{aligned} \Delta I(\mathbf{x}, \mathbf{h}) \;=\; & \sum_{\mathbf{x}_s}\sum_{\omega} \Big(\overline{\Delta D(\mathbf{x} - \mathbf{h}, \mathbf{x}_s)}\widehat{U}(\mathbf{x} + \mathbf{h}, \mathbf{x}_s) + \\ & \overline{\widehat{D}(\mathbf{x} - \mathbf{h}, \mathbf{x}_s)}\Delta U(\mathbf{x} + \mathbf{h}, \mathbf{x}_s)\Big), \end{aligned} \tag{11}$$

where $\widehat{D}(\mathbf{x}-\mathbf{h}, \mathbf{x}_s)$ and $\widehat{U}(\mathbf{x}+\mathbf{h}, \mathbf{x}_s)$ are the background source and receiver wavefields computed with the background model $\widehat{Q}(\mathbf{x})$, and $\Delta D(\mathbf{x}-\mathbf{h}, \mathbf{x}_s)$ and $\Delta U(\mathbf{x}+\mathbf{h}, \mathbf{x}_s)$ are

the perturbed source wavefield and perturbed receiver wavefield, respectively, which result from the model perturbation $\Delta Q(\mathbf{x})$.

To evaluate the adjoint tomographic operator $\mathbf{T}^*$, which backprojects the image perturbation into the model space, I first compute the wavefield perturbation from the image perturbation using the adjoint imaging condition:

$$\begin{aligned} \Delta D(\mathbf{x},\mathbf{x}_s) &= \sum_{\mathbf{h}} \Delta I(\mathbf{x},\mathbf{h}) \widehat{U}(\mathbf{x}+\mathbf{h},\mathbf{x}_s) \\ \Delta U(\mathbf{x},\mathbf{x}_s) &= \sum_{\mathbf{h}} \Delta I(\mathbf{x},\mathbf{h}) \widehat{D}(\mathbf{x}-\mathbf{h},\mathbf{x}_s). \end{aligned} \tag{12}$$

The perturbed source and receiver wavefields satisfy the following one-way wave equations, linearized with respect to Q:

$$\begin{cases} \left(\frac{\partial}{\partial z} + ik_z\right) \Delta D(\mathbf{x},\mathbf{x}_s) = \left(-i\frac{\partial k_z}{\partial Q}\widehat{D}(\mathbf{x},\mathbf{x}_s)\right) \Delta Q(\mathbf{x}) \\ \Delta D(x,y,z=0,\mathbf{x}_s) = 0 \end{cases}, \tag{13}$$

and

$$\begin{cases} \left(\frac{\partial}{\partial z} - ik_z\right) \Delta U(\mathbf{x},\mathbf{x}_s) = \left(-i\frac{\partial k_z}{\partial Q}\widehat{U}(\mathbf{x},\mathbf{x}_s)\right) \Delta Q(\mathbf{x}) \\ \Delta U(x,y,z=0,\mathbf{x}_s) = 0 \end{cases}, \tag{14}$$

When solving the optimization problem, I obtain the image perturbation by comparing the background image and the target image. Then the perturbed image is convolved with the background wavefields to get the perturbed wavefields (Equation 12). The scattered wavefields are computed by applying the adjoint of the one-way wave-equations 13 and 14. Finally, the perturbation $\Delta Q(\mathbf{x})$, is obtained by cross-correlating the upward-propagated scattered wavefields with the modified background wavefields,

$$\Delta Q(\mathbf{x}) = \sum_{x_s} \sum_{\omega} \overline{\Delta D} \left(-i\frac{\partial k_z}{\partial Q}\widehat{D}\right) + \overline{\Delta U} \left(-i\frac{\partial k_z}{\partial Q}\widehat{U}\right). \tag{15}$$

Image perturbation estimation

As definition, the image perturbation $\Delta\mathbf{I}$ is the difference between the background image $\mathbf{I}$, computed with the current background Q model, and the 'target' image, $\hat{\mathbf{I}}$;which is an attenuation-free image. In fact, instead of computing the difference between these two images, we calculate the spectral change of the images. The change in the spectrum can be indicated by the steepness of the slope computed by `spectral ratio` method (Tonn, 1991). The larger slope demonstrates more frequencies are

attenuated. As attenuation is a frequency-dependent amplitude effect, the intercept calculated from `spectral ratio` method removes the frequency-independent amplitude effects, such as geometric spreading, instrument response, source/receiver coupling, radiation patterns, and reflection/transmission effects. Therefore, the perturbed image are measured from the perturbed amplitude spectral change after the absolute scaling of the waveform has been removed.

In this section, we develop ways of measuring the image perturbation for two scenarios: the model with sparse reflectors and the model with dense reflectors. The choice of the target image $\widehat{\mathbf{I}}$ is the main distinguishing element between these two different measurements of the perturbed image. Both of these methods require accurate velocity models. Fortunately, since both velocity and Q model building share the same tomography kernel, we can updated these two models simultaneously.

Model with sparse reflectors

As the reflectors are sparsly distributed in the subsurface, we assume those reflectivities are white and can be picked from the background image. Therefore, the target image $\widehat{\mathbf{I}}$ in this method is the image of a non-attenuated dataset generated by a set of picked reflectivities. We design an automatic picker to pick each individual event for spectrum analysis and target image generation. The picker automatically pinpoints the local maximum of the envelope of each trace and places a normalized reflectivity R on the reflector. During this procedure, thresholding helps choose the reflector with relatively high amplitude. We synthesize a set of non-attenuated data by injecting the known source wavelet into a non-attenuated medium with reflectivity R. This data is then remigrated to obtain the non-attenuated target image $\widehat{\mathbf{I}}$. In the real case, not all of the reflectivities can be accurately picked. Therefore, only key reflectors are selected to generate the target image $\widehat{\mathbf{I}}$. An image mask $\mathbf{M}$ is needed to select the corresponding reflections in background image $\mathbf{I}$, and $\mathbf{M}$ is designed according to the energy of the target image $\widehat{\mathbf{I}}$.

Model with dense reflectors

For some real cases, events are very close to each other, so that they will be difficult to individually separate. The interference of those events may introduce errors into spectral analysis. Therefore, instead of comparing the frequency contents of each events, we compare the spectral difference between an amount of selected windowed events from the background image with the events in the reference windows. These reference windows are calfully selected from the background image so that they are not contaminated by attenuation and can be used as our target image. All the windows in this method are in the large and same size, hence the influence of the interferenced reflectivies on the spectra are statistically the same over windows. Based on the assumption that the amplitude spectra contain the same frequency contents over windows if the Q model for imaging is accurate, this method minimizes the spectral differences between the selected windows and the reference windows.

EXAMPLES

Numerical test of downward-continuation imaging with Q

To test the downward continuation operator with Q, we run downward-continuation imaging with Q on a 2-D model. The model size is 4000 m (length) x 2500 m (depth). A horizontal reflector is at 1500 m depth, and 51 sources and 401 receivers are uniformly distributed on the surface. The medium is homogeneous with constant velocity (2000 m/s) and constant Q (50 for the model with attenuation and 99999 for the model without attenuation). A Ricker wavelet with 50 Hz central frequency is used as the source wavelet.

For conveniently comparing the wavelets in Figure 1, all plots are displayed in normalized wiggles, and the maximum amplitude of those wavelets before normalization are presented in the title. Figure 1(a) shows the conventional migration of the data generated from the model without attenuation, which images the reflector at 1500m depth. Figure 1(b), and Figure 1(c) shows the conventional migration, and migration compensated by the true Q model of the data generated from the model with attenuation, respectively. Due to the higher-frequency frequencies loss and velocity dispersion caused by attenuation, the wavelets in Figure 1(b) are stretched, amplitude-decayed and phase-rotated when compared with Figure 1(a). Figure 1(c) shows exactly the same result as Figure 1(a), indicating that Q compensation adequately restores both the amplitude and phase.

Numerical test of the wave-equation Q tomography operator

Similar to the forward tomographic operator in WEMVA (Sava and Biondi, 2004; Biondi, 2006) that linearizes the image around the velocity, the forward wave-equation Q tomography operator relates the perturbation in Q to the image perturbation by linear approximation. This approximation may fail when the model error is large. To verify the effectiveness of this linear approximation, I compare the results generated by the linearized operator and the non-linearized image perturbation that is obtained by subtracting the background image from the true image. The size of the test 2D model is 4000 m (length) x 1200 m (depth). A horizontal reflector is at 900 m depth, and 51 sources and 401 receivers are uniformly distributed on the surface. The background medium is homogeneous with constant velocity (2000 m/s) and no attenuation ($Q = 10000$). Figure 4(a) shows the model perturbation with rectangular low Q. The Q errors are set to 5%, 10%, 20%, 30%, 40%, 50%, 60%, 70%, 80% and 90% lower than the background model.

I compare the linearized and the non-linearized image perturbation by examining their RMS value. Figure 2 shows their RMS values as ΔQ increases. The results show that this wave-equation Q tomography operator is a good linear approximation when Q error is less then 50%, but fails in approximating the non-linearized image perturbation when the model error increases.

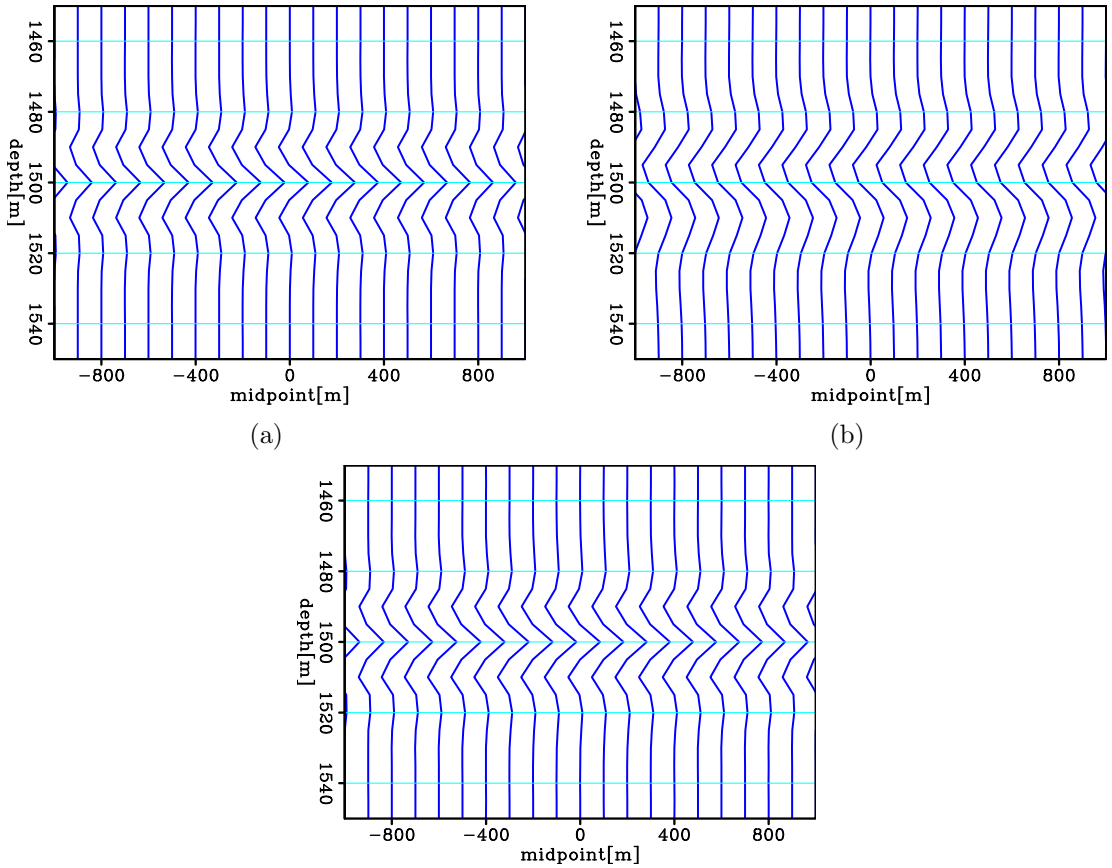

Figure 1: For convenient comparison the wavelets, all plots are in normalized wiggles. (a) Conventional migration on non-attenuated data. The maximum amplitude of the event before normalization is 0.28; (b) conventional migration on attenuated data. The maximum amplitude of the event before normalization is 0.0015; (c) migration compensated by the true Q model on attenuated data. The maximum amplitude of the event before normalization is 0.27. [**ER**]

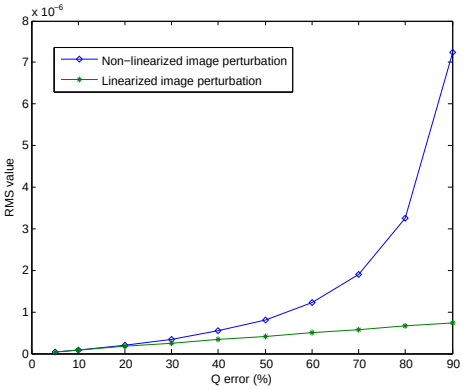

Figure 2: The linearized and the non-linearized image perturbation are compared by examining their RMS value. This figure shows their RMS values as ΔQ increases. The results show that this wave-equation Q tomography operator is a good linear approximation when Q error is less then 50%, but fails in approximating the non-linearized image perturbation when the model error increases. [**CR**]

To test the adjoint of the wave-equation Q tomography operator $\mathbf{T}^*$, I run it in a homogeneous background medium with $v = 2000$ m/s and $Q = 50$. The input of the adjoint tomographic operator is a spike in the image space $\Delta\mathbf{I} = \delta$ ($x = 0$ m, $z = 900$ m). Figure 3(a) and Figure 3(b) show the back-projected Q gradient where the source-receiver offset is 0 km and 1.6 km respectively. Clearly, these back projections have a banana-donut shape and are spread along the wavepaths from the source to the perturbed image point and from the perturbed image point to the receiver.

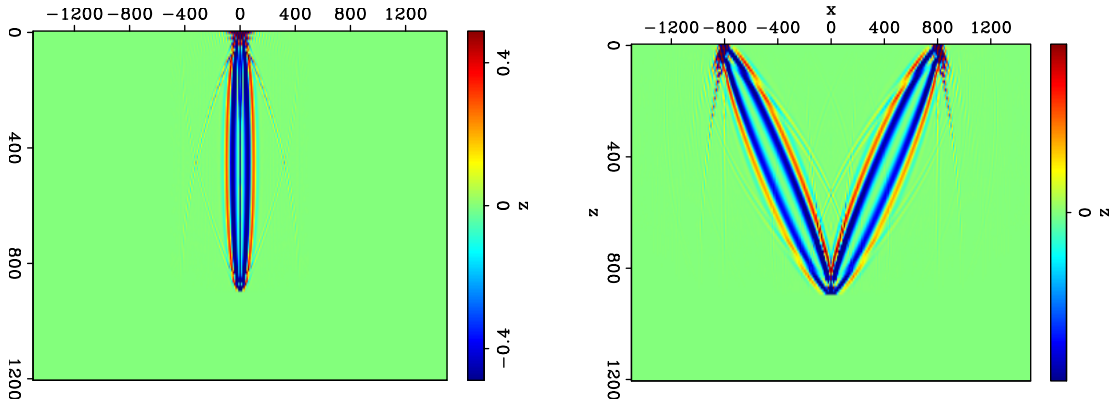

(a) (b)

Figure 3: 2D impulse responses for Q: (a) zero-offset impulse responses; (b) impulse responses when source-receiver offset is 1.6 km. [**ER**]

Numerical tests on the model with sparse reflectors

This section applies WEMQA to two 2-D synthetic examples to update an inaccurate Q model. The size of the first test 2D model is 4000 m (length) x 1200 m (depth). A horizontal reflector is at 900 m depth, and 51 sources and 401 receivers are uniformly distributed on the surface. The background medium is homogeneous with constant velocity (2000 m/s) and constant Q ($Q = 50$). A Ricker wavelet with 50 Hz central frequency is used as the source wavelet. Figure 4(a) and Figure 4(b) show the true Q models, which have a Q anomaly of 10% lower and higher than the background, respectively.

We model the data using the true Q model (the background plus the perturbation), and use the background Q model as the initial model. After migration on the attenuated data with the initial Q model, the reflectivities are automatically picked from the background image that serve as the input for the target image. Figure 4(c) and 4(d) shows the image perturbation obtained by subtracting the background image from the target image. These images have larger perturbation underneath the Q anomaly than in the area far away from the anomaly. In addition, the sign of the amplitude of the middle lobe of the reflector in Figure 4(c) and 4(d) indicates the direction for updates. The positive amplitude of the middle lobe of the reflector in

Figure 4(c) indicates the background image is undercompensated, and smaller Q is needed for the updates. The reverse is true for Figure 4(d). Figure 4(e) and 4(f) shows the inversion results using steepest descent algorithm after 3 iterations. The results show that both the shape and the values of the Q anomalies are recovered.

The second test example is modeled on a realistic subsurface structure with an absorptive gas cloud. Figure 5(a) shows the velocity model with multiple reflectors, and Figure 5(b) presents a Gaussian Q anomaly in a non-attenuating medium. The data are modeled with 3 km maximum offset, 10 m receiver spacing, 40 m source spacing, and a 50Hz Ricker wavelet. We use a non-attenuating medium as the initial model. Figure 5(c) show the inversion results using steepest descent algorithm after 4 iterations. As the initial model is far from the true model, the low Q anomaly is partially recovered in Figure 5(c), and hence more iterations are needed to better retrieve the true model.

Numerical tests on the model with dense reflectors

A part of a modified SEAM velocity model is used in this section. This model includes two gas clouds with lower velocity than the surrounding sediments (Figure 6(a)). The Q model shown in Figure 6(b) also has these two gas clouds with high attenuation. We generate synthetic data with 51 shots with 0.2km spacing, 251 receivers with 0.04km spacing, and a Ricker wavelet with 50 Hz central frequency. The initial model to the inversion is a model without attenuation. After migration on the attenuated data with the current Q model, we generate the image perturbation by calculating the slope of the logarithm of the spectral ratio between the windowed events of each trace and the events in the reference window. The window size is 3km, and 30 sliding windows are used for each trace. The reference windows are in x=6km, which are not contaminated by attenuation. As both the structures and velocities in this example does not have strong horizontal variation, the compared windows and the reference windows are in the same depth. Figure 6(c) show the inversion results using steepest descent algorithm after 2 iterations. The results indicates the accurate locations of these two anomalies. However, the energy around these anomaly is strong. As for the gas clouds, the initial model is 90% far from the true model, which makes the wave-equation tomographic operator fails in linear approximation and emphasizes the side-lobes. Therefore, we need more iterations to better retrieve the anomalies.

CONCLUSION

We design a new method –WEMQA to produce reliable Q models. This method is performed in the image-space, which uses downward-continuation imaging with Q to stack out noise, focus and simplify events, and provide a direct link between the model perturbation and the image perturbation. We develop two methods to generate the image perturbation for the following scenarios: the model with sparse reflectors

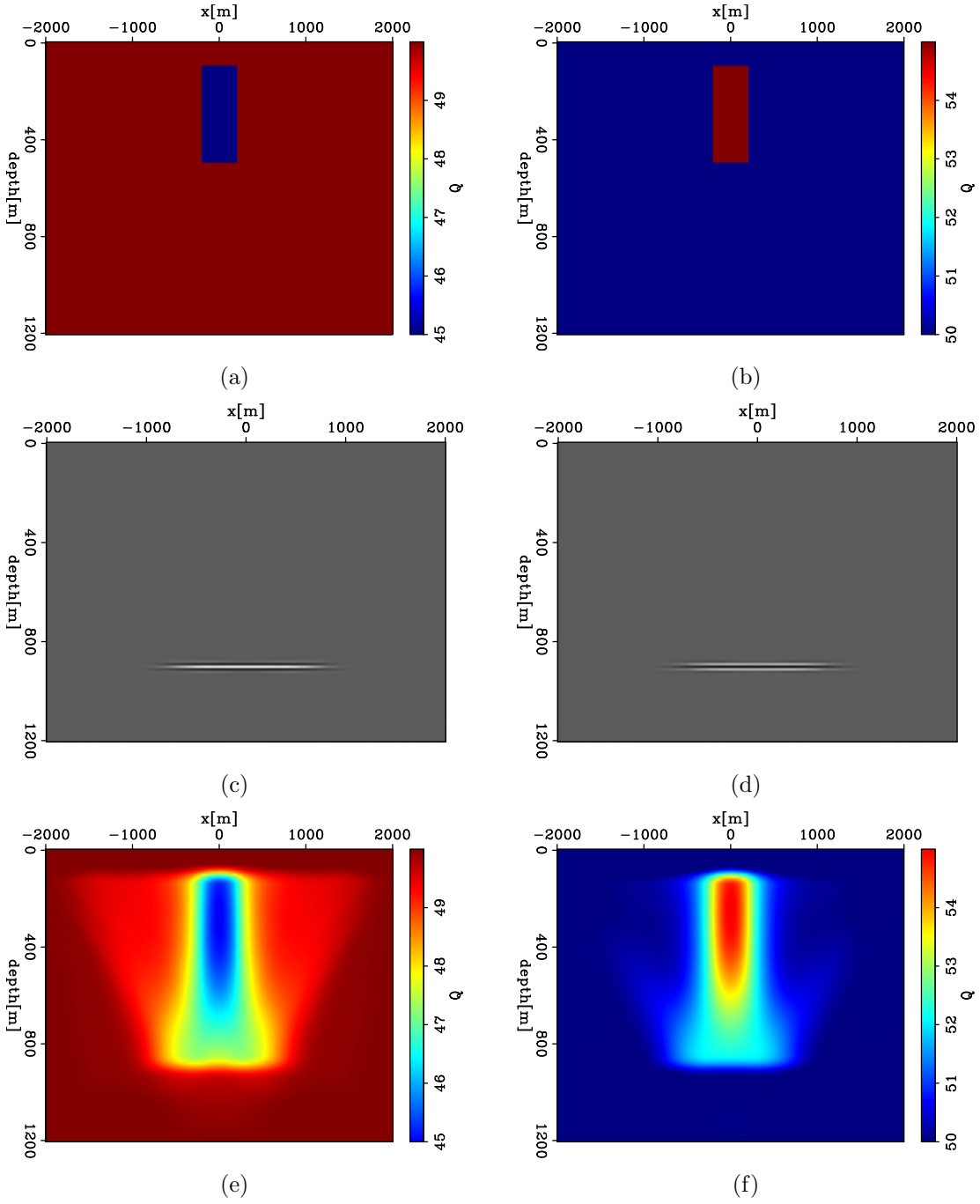

Figure 4: Q perturbations: (a) rectangular Q anomaly that is 10% lower than the background Q; (b) rectangular Q anomaly that is 10% higher than the background Q; (c) image perturbation caused by the perturbed model in Figure 4(a); (d) image perturbation caused by the perturbed model in Figure 4(b); (e) inversion results of the low Q anomaly shown in Figure 4(a) using steepest descent algorithm after 3 iterations; (f) inversion results of the high Q anomaly shown in Figure 4(b) using steepest descent algorithm after 3 iterations. [**ER**]

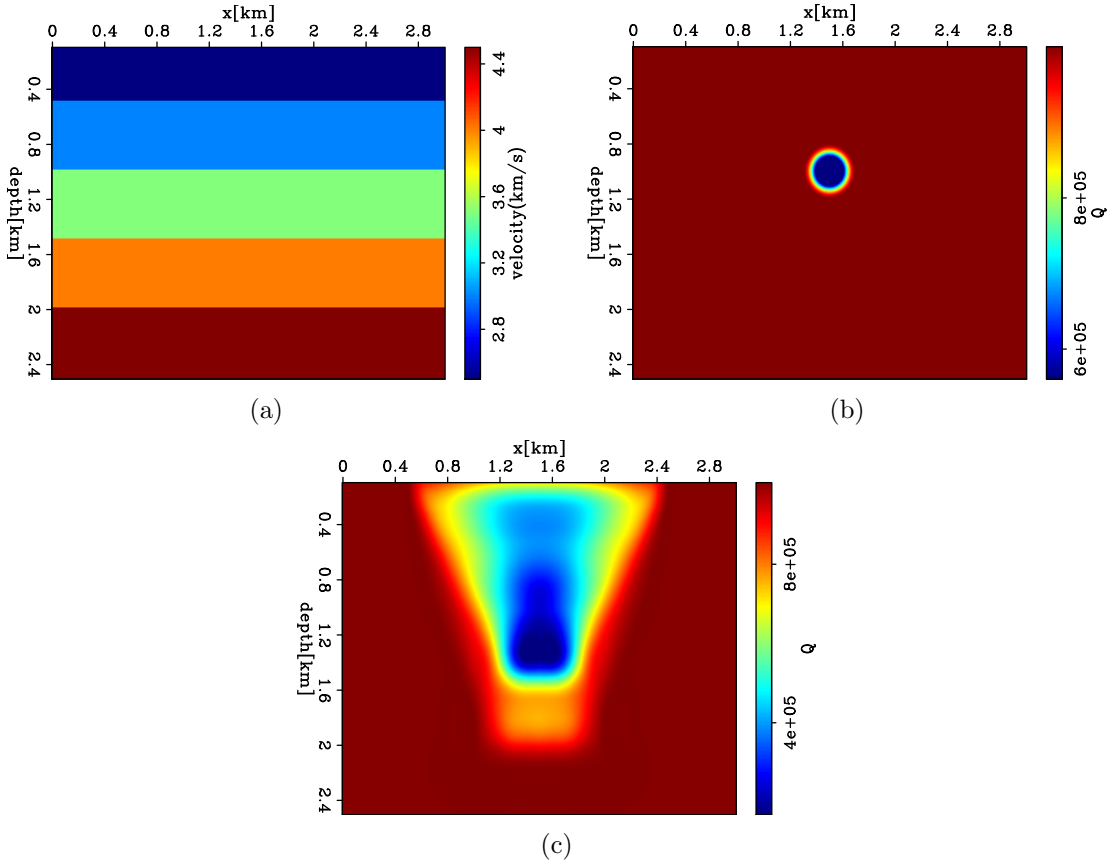

Figure 5: (a) True velocity model with multiple reflectors; (b) True Q model with a Gaussian anomaly in a non-attenuating medium. (c) Inverted Q model using steepest descent algorithm after 4 iterations. [**ER**]

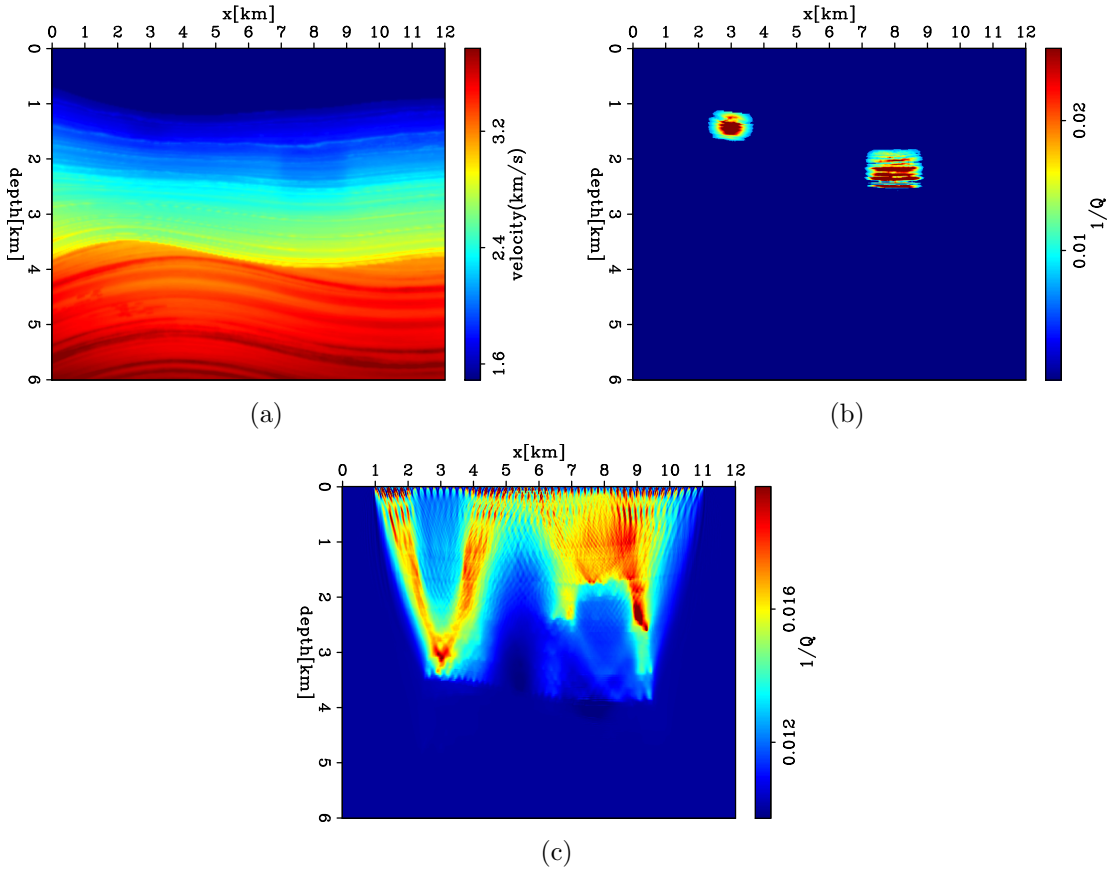

Figure 6: (a) A part of a modified SEAM velocity model with two gas clouds. ; (b) True Q model with two gas clouds. (c) Inverted Q model using steepest descent algorithm after 2 iterations. [**ER**]

and the model with dense reflectors. Second, this method uses wave-equation Q tomography to handle the complex wave propagation. Two synthetic tests on two different 2-D models with a Q anomaly shows the capability of this method on the model with sparse events. Tests with a modified SEAM model also demonstrate the feasibility of this method for the model with dense events.

ACKNOWLEDGMENTS

The authors thank Biondo Biondi, Robert Clapp and Dave Nichols of Stanford for their advice and suggestions, and also thank Yunyue Li, Ali Almomin and Sjoerd de Ridder for fruitful discussion.

REFERENCES

Best, A. I., C. MaCann, and J. Sothcott, 1994, The relationships between the velocities, attenuations, and petrophysical properties of reservoir sedimentary rocks: Geophysical Prospecting, **42**, 151–178.

Biondi, B. L., 2006, 3-D seismic imaging.

Brzostowski, M. A. and G. A. McMechan, 1992, 3-D tomographic imaging of near-surface seismic velocity and attenuation: Geophysics, **57**, 396–403.

Claerbout, J. F., 1971, Towards a unified theory of reflector mapping: Geophysics, **36**, 467–481.

Dasgupta, R. and R. A. Clark, 1998, Estimation of Q from surface seismic reflection data: Geophysics, **63**, 2120–2128.

Futterman, W. I., 1962, Dispersive body waves: Journal of Geophysical Research, **67**, 5279–5291.

Kjartansson, E., 1979, Constant Q wave propagation and attenuation: Journal of Geophysical Research, **84**, 4737–4748.

Leaney, W. S., 1999, Walkaway Q inversion: 69th Annual International Meeting, SEG, Expanded Abstracts, 1311–1314.

Leggett, M., N. R. Goulty, and J. E. Kragh, 1992, Study of traveltime and amplitude time-lapse tomography using physical model data: Abstracts of 54th EAEG Meeting,, 248–249.

Mateeva, A., 2003, Thin horizontal layering as a stratigraphic filter in absorption estimation and seismic deconvolution: PhD thesis, Colorado School of Mines.

Plessix, R. E., 2006, Estimation of velocity and attenuation coefficient maps from crosswell seismic data: Geophysics, **71**, S235–S240.

Quan, Y. and J. M. Harris, 1997, Seismic attenuation tomography using the frequency shift method: Geophysics, **62**, 895–905.

Reine, C., R. A. Clark, and M. van der Baan, 2012a, Robust prestack Q-determination using surface seismic data: Part 1 Method and synthetic examples: Geophysics, **77**, R45–R56.

———, 2012b, Robust prestack Q-determination using surface seismic data: Part 2 3D case study: Geophysics, **77**, B1–B10.

Rickett, J., 2006, Integrated estimation of interval-attenuation profiles: Geophysics, **71**, A19–A23.

———, 2007, Estimating attenuation and the relative information content of amplitude and phase spectra: Geophysics, **72**, R19–R27.

Sava, P. and B. Biondi, 2004, Wave-equation migration velocity analysis-i: Theory: Geophysical Prospecting, **52**, 593606.

Tonn, R., 1991, The determination of seismic quality factor Q from VSP data: A comparison of different computational techniques: Geophysical Prospecting, **45**, 87–109.

Valenciano, A. A., N. Chemingui, D. Whitmore, and S. Brandsberg-Dahl, 2011, Wave equation migration with attenuation and anisotropy compensation: 2011 Annual Meeting, SEG, Expanded Abstracts, 232–236.

Zucca, J. J., L. J. Hutchings, and P. W. Kasameyer, 1994, Seismic velocity and attenuation structure of the geysers geothermal field, california: Geothermics, **23**, 111–126.